

Evaluating Porosity in Cordierite Diesel Particulate Filter Materials, Part 1 X-Ray Refraction

A. Kupsch, A. Lange, M.P. Hentschel, Y. Onel, T. Wolk,
A. Staude, K. Ehrig, B. R. Müller, G. Bruno*

BAM Federal Institute for Materials Research and Testing, D-12200 Berlin, Germany
received August 23, 2013; received in revised form October 18, 2013; accepted November 18, 2013

Abstract

Bi-continuous porous ceramics for filtration applications possess a particularly complicated microstructure, with porosity and solid matter being intermingled. Mechanical, thermal, and filtration properties can only be precisely estimated if the morphology of both solid matter and porosity can be quantitatively determined. Using x-ray absorption and refraction, we quantitatively evaluate porosity and pore orientation in cordierite diesel particulate filter ceramics. Porosity values turn out to agree with mercury intrusion measurements, while pore orientation factors agree with published crystallographic texture data.

Keywords: Porous ceramics, pore orientation, x-ray refraction, synchrotron, interface.

I. Introduction

Porous synthetic cordierite is an attractive ceramic material commonly used for Diesel Particulate Filters (DPFs) ¹ and refractories ^{2,3}. Among its properties, the anisotropy of the thermal expansion (see for example Bruno *et al.* ⁴) is widely used to tailor the thermal and mechanical properties ⁵. In fact, monoliths for DPF applications are commonly extruded, and the grains (or to be more precise, the domains ^{6,7}) tend to align with their negative expansion crystallographic axis along the filter extrusion direction.

The degree of crystallographic grain alignment is not particularly high ^{7,8} (texture factors of typically 1.2–1.3), yet it is sufficient to bring about very low axial thermal expansion, and consequently high thermal shock resistance ⁹. These attractive axial properties are accompanied by relatively poor transverse properties ¹⁰, which can cause complex stress states. In general, it is not clear whether the mechanical properties (above all Young's modulus) are influenced by the crystal texture: while from one side it has been demonstrated that microcracking preferentially occurs along the highest thermal expansion axis (this has been observed for aluminum titanate ¹¹ and β -eucryptite ¹²), very little data is available on the transverse mechanical properties. Shyam *et al.* ¹³ report anisotropy of the thermal expansion, but do not mention similar effects for fracture toughness and Young's modulus; Gulati ¹⁰ shows that the axial-to-transverse ratio of Young's modulus measured by sonic resonance ¹⁴ simply satisfies a geometrical law (i.e. owing to the cellular geometry).

Besides the properties of the solid phase, one of the most important features to take into account when evaluating the performance of these materials is the pore mor-

phology, and consequently, the pore orientation. Firstly, from a micromechanical standpoint, the pore morphology factor ^{15,16} is a decisive quantity to determine the effective mechanical properties. Furthermore, Kachanov ¹⁷ has clearly shown that the relevant microstructural parameters to determine elastic and conductive properties in porous microcracked materials are the porosity tensor (second rank), and the crack density tensor (fourth rank). Secondly, in Kachanov's works (see also ¹⁸) it is also mentioned that permeability depends on the pore structure, although the permeability tensor does not have the same symmetry of the elastic and conductive tensors. Indeed, the filtration efficiency of a DPF represents its most important functional attribute ^{19,20}.

It is therefore clear that proper characterization of the pore orientation in a bi-continuous medium such as a DPF is of paramount importance. Yet, the most common method of characterization (if not the only one in the industrial community) is still mercury intrusion. Now, mercury intrusion (as well as similar techniques, such water intrusion ²¹) rests on the Washburn's relation ^{22,23}, thereby assuming cylindrical pores. This assumption is unacceptable in bi-continuous media with almost exclusively open porosity, and alternatives need to be sought. Image analyses of 2D scanning electron microscope (SEM) pictures or 3D tomograms ²¹ are a practical way to tackle the problem of the determination of pore orientation, which, however, may suffer from limited field of view (especially for SEM).

X-ray refraction ²⁴ is a structural characterization method based on the geometrical optical refraction of x-rays, which has already been demonstrated for the quantification of porosity ²⁵, thanks to its sensitivity to specific (internal) surface. This technique has been utilized successfully for the microstructural evaluation of both solid

* Corresponding author: giovanni.bruno@bam.de

matter and porosity in two-phase composites²⁶. In²⁶ both 3D and 2D methods were used to identify the microstructural components. In this work we shall show how this technique, combined with simple image analysis, can yield significant insight into the *quantitative* measurement of pore orientation in DPFs, without any assumption with regards to the pore morphology.

II. Materials

Two commercial cordierite DPF ceramic honeycomb filter materials were used in this work (see Fig. 1). Small samples for x-ray refraction experiments were extracted from larger pieces. We used single wall slabs of about 1 cm² in area, and small cubes of about 1 cm³ in volume (thus containing several honeycomb cells). The honeycomb materials were cordierite-based, produced by means of extrusion of a mixture of talc, kaolin, alumina, silica, and pore formers, and firing at a temperature in excess of 1400 °C. Similar materials have been characterized in other works^{13,27}. Samples (indicated with S1 and S2) have about 62 % and 50 % porosity, with 10 μm and 18 μm median pore diameter, respectively, as determined by an Autopore 9200 (Micromeritics, Norcross, GA, USA). The coefficients of thermal expansion (CTE, between room temperature and 1000 °C) are about 1.1 and 0.6 × 10⁻⁶ °C⁻¹, respectively for S1 and S2 (as determined with a Netzsch DIL 402C dilatometer). Note that the “median pore diameter” may differ considerably from the “average pore diameter”, if the distribution is asymmetric. The sample properties are summarized in Table 1.

Table 1: Selected properties of the cordierite samples.

Sample	Porosity (%)	Median Pore Diameter/μm	CTE (RT-1000 °C) 10 ⁻⁶ °C ⁻¹
S1	62	10	1.15
S2	50	18	0.57

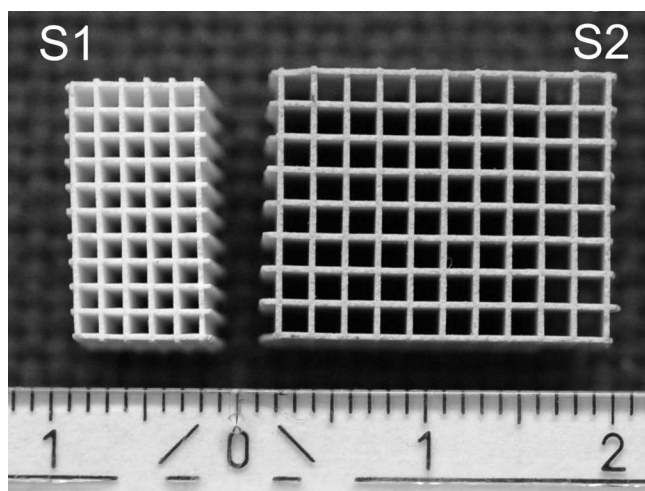


Fig. 1: Photograph of samples S1 (white) and S2 (light brown). Scale bar in mm.

These materials can be considered prototypical of all DPF cordierite-based materials, and therefore all properties available in the open literature^{13,4,28} approximately apply. In particular, the results shown in^{13,29,30} as well as in^{31,32} exemplify the mechanical and thermal properties, as well as the microstructure of these materials. For reference, an SEM image of sample S2 is shown in Fig. 2.

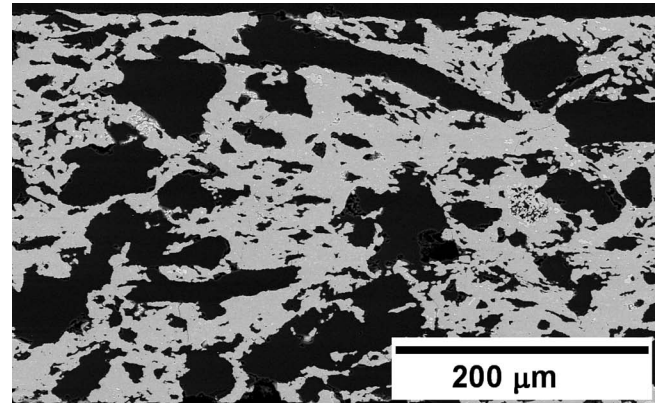


Fig. 2: SEM image of sample S2. A whole wall thickness of the honeycomb is shown.

III. Experimental Techniques

(1) X-ray refraction

In analogy to the well-known refraction of visible light with optical lenses and prisms, the physics of x-ray refraction follows Snell’s law. The major difference to visible light is that the refractive index *n* of x-rays in matter is slightly smaller than 1. This causes ray deflections of very small angles (up to a few minutes of arc). While higher porosity (*p*) causes an increased transmission signal (conventional radiometric porosity measurements are based on attenuation), the refractive scattering signal is larger with increasing internal specific surface.

The experimental equipment consists of a standard fine structure x-ray generator providing monochromatic radiation. The refraction effect is measured using a commercial small-angle scattering x-ray camera of the Kratky type³³ in combination with two scintillation detectors. This allows simultaneous detection of the x-ray refraction intensity *I_R*, and of the sample absorption *I_A* (see Fig. 3 for the schematics of the experiment).

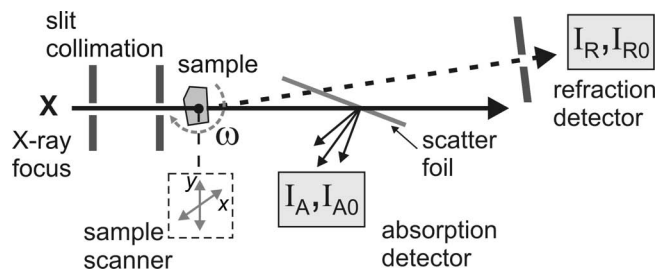


Fig. 3: Instrumental laboratory set-up for simultaneous 2-dimensional detection of porosity *p* and internal specific surface *Σ*. The detected x-ray refraction scattering angles are fixed to a lower limit of 2.5 minutes of arc and include all larger ones. Sample scanning can be done in a plane perpendicular to the primary beam. The scattering plane corresponds to the plane of the drawing.

If the linear attenuation coefficient μ and the sample thickness d are known, the transmitted intensity I_A (with sample) and I_{A0} (without sample) permit the determination of the porosity p :

$$\mu \cdot d = \ln(I_{A0} / I_A) / (1 - p) \quad (1)$$

It should be pointed out that the values I_R and I_A , together with the sample thickness d , are sufficient to determine all essential microstructural parameters, particularly with regard to the evaluation of the internal specific surface Σ (surface per unit volume)³⁴. In particular, we can calculate the quantity

$$C_m \cdot d = \frac{I_R / I_{R0}}{I_A / I_{A0}} - 1 \quad (2)$$

C_m is referred to as the *refraction value* of a material. It represents a relative measure for the internal specific surface Σ . In our case, this internal surface will be dominated by pore surfaces, but it will also contain microcrack surfaces (oriented perpendicular to the scattering plane), and interphase grain boundaries (whereby the x-ray refractive index n has a substantial jump). Therefore in the following the specific surface Σ will be referred to as the *defect specific surface*.

(2) Refraction two-dimensional scanning

The refraction signal is always integrated over the sample thickness. However, it is possible to obtain position-dependent information on the two quantities determined above (porosity and defect specific surface). Two-dimensional (2D) sample scanning (also referred to as *topography* in the literature³⁴) was performed in steps of $\Delta x = 250 \mu\text{m}$ and $\Delta y = 125 \mu\text{m}$. The I_A value was used to determine the local porosity p at sampling position (x, y) , and the combination of I_A and I_R (Eq.(2)) yielded the specific defect surface at the same position. As mentioned above, each pixel in the two-dimensional images of porosity and specific surface, $p(x, y)$ and $\Sigma(x, y)$, represents a through-thickness mean value. A personal computer stored and processed the scattered intensity data and controlled the sample scanning system. A scheme of the experimental set-up is shown in Fig. 3. We used $\text{CuK}\alpha$ radiation (8 keV), with a beam cross-section of $400 \mu\text{m} \times 400 \mu\text{m}$ and a measurement time of 1 sec per sampling point. The overlap of the sampling points allowed us to increase statistics.

(3) Refraction 2D tomography

Beyond 2D refraction position scanning, an extended experimental set-up was employed, allowing 2D computed tomography (CT)^{35,36}. This set-up was designed to gain in-depth information on the specific surface of these porous materials³⁶. Various techniques of *synchrotron* CT have been developed, exploiting advanced imaging techniques such as Diffraction Enhanced Imaging (DEI)³⁷, Talbot-Lau grating interferometry³⁸ or Refraction Enhanced Imaging (REI)³⁹. Moreover, the refraction contrast has been applied to *neutron* imaging^{40, 41} and tomography⁴². Nevertheless, even laboratory equipment can provide direct access to internal interfaces by means of 2D refraction CT.

The experimental set-up for 2D refraction shown in Fig. 3 was modified with an additional rotation device with a horizontal axis ω (perpendicular to the incident beam direction, see Fig. 3). This provided the required sample rotation to perform CT measurements. Vertical line scans ($50 \mu\text{m}$ steps) were performed for each angle of sample orientation (angular increments of 1 deg about 360 deg). In order to increase transmitted intensity for this sample geometry, a hard radiation ($\text{MoK}\alpha$ of 17.5 keV) was used. The primary beam cross-section measured about 1.5 mm (horizontal) by $50 \mu\text{m}$ (vertical). This implies that the 2D images were actually pseudo-3D, being integrated over 1.5 mm length along the extrusion axis.

The typical measurement time for one slice was a few hours. We measured five single slices, without detecting any considerable signal variation among them; therefore, only one example slice will be shown in the following.

(4) Synchrotron refraction radiography

In addition to the lab refraction 2D scanning measurements, the technique of synchrotron refraction radiography³⁵ was used.

The experimental set-up is illustrated in Fig. 4, and the set-up parameters used in this work are shown in Table 2. A (virtually) monochromatic spectral line was selected from the white synchrotron light by means of a double-crystal monochromator. In order to avoid detector back-light effects^{43, 44}, the beam cross-section was narrowed with three slit systems, to fit the actually used field of view. After interacting with the sample, the transmitted beam was diffracted by an analyzer crystal. This enabled: a) separation of the incident (and forward transmitted) beam from the scattered one, according to the DEI principle, see³⁷: scattering at very small angles (about a few seconds of arc) was entirely suppressed, within the width of the Darwin-Prins rocking curve of the analyzer crystal; and b) separation of the contributions from different spatial locations within the sample. Contrary to the laboratory set-up, sample scanning was not required owing to direct imaging on the 2D CCD detector (obviously, after conversion to visible light by a fluorescent screen).

Table 2: Parameters of the synchrotron set-up used in this work.

Energy (keV)	15.0 ± 0.15
Monochromator	Si (111), double crystal
Filters	1 mm Al, $50 \mu\text{m}$ Cu
Sample-analyzer distance (mm)	100
Analyzer crystal	Si (111), symmetric
Fluorescent screen (scintillator)	$20 \mu\text{m}$ CdWO_4 on quartz glass ($\varnothing 22 \text{ mm}$)
Objective	Rodenstock, $f = 100 \text{ mm}$, eff. pixel size $7 \mu\text{m}$
Camera	Princeton Instruments 2048×2048

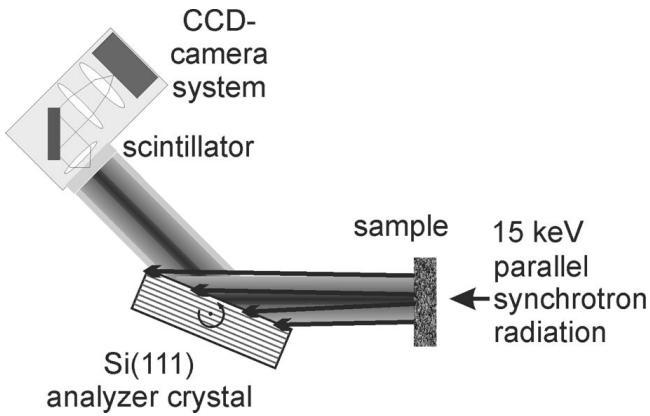


Fig. 4: Set-up of synchrotron refraction radiography (monochromatic mode). In the sketch, the dark-shaded (attenuated) primary beam portions are diffracted by the analyzer crystal. The black-arrowed rays (scattered by the sample) do not fulfill the Bragg condition, and thus are not reflected by the crystal and not detected by the camera system. The scattering plane corresponds to the plane of the drawing.

IV. Results and Discussion

Two-dimensional (2D) refraction images (also called topographs in the existing literature) of single wall slabs of both cordierite samples in two different sample orientations are shown in Fig. 5. Those images were built taking the measured transmitted and refracted x-ray intensities, and using Eqs. 1 and 2. The large slab was prepared from sample S1, the small slab from S2. Images 5a to c were taken with the scattering vector q nearly parallel to the extrusion axis, images d to f were acquired with the extrusion direction normal to the scattering plane (see also Fig. 3 for help). Images 5a and d show a 2D map of the absorbing mass in the samples (absorption coefficient \times thickness), or in other words the density distribution, calculated from the transmit-

ted intensity; images b and e show an analogous map of the refraction value C_m , calculated from the refracted intensity (Eq. 2), and therefore yield information on the defect specific surface; images c and f display the ratio of the quantities in Figs. 5a to b and d to e, i.e., the ratio between the scattered and the transmitted signal. This ratio yields information on the specific surface normalized to the local porosity, and is therefore independent of the sample thickness. Footprints of perpendicular walls (cut away during sample preparation) can be easily seen as brighter horizontal lines. Note that the defect specific surface normalized by the porosity is more homogeneously distributed than the absorption coefficient μ and the refraction value C_m .

The samples' gray levels in Figs. 5a and d clearly show that the absorption in sample S2 is stronger owing to higher density and larger wall thickness. Sample S2 also shows a higher degree of specific surface inhomogeneity (Figs. 5b and e), both within the walls and in the regions corresponding to the ground protruding walls (perpendicular to the image plane). This would imply a larger pore size distribution, if we talk in classic mercury porosimetry terms. Indeed, the mercury intrusion plots (Fig. 6) show that Sample S1 possesses a smaller full width at half maximum of the pore distribution. Although this result is purely qualitative, it shows that x-ray refraction data are fully compatible with classic methods (see also 25). Mercury intrusion cannot give a correct pore size since for these materials it is virtually impossible to define a pore shape. In our case mercury intrusion is used as a 'sanity check'. Figs. 5c and f show a higher defect specific surface (normalized by porosity) for S1. This again implies that S1 possesses smaller defects (mostly pores).

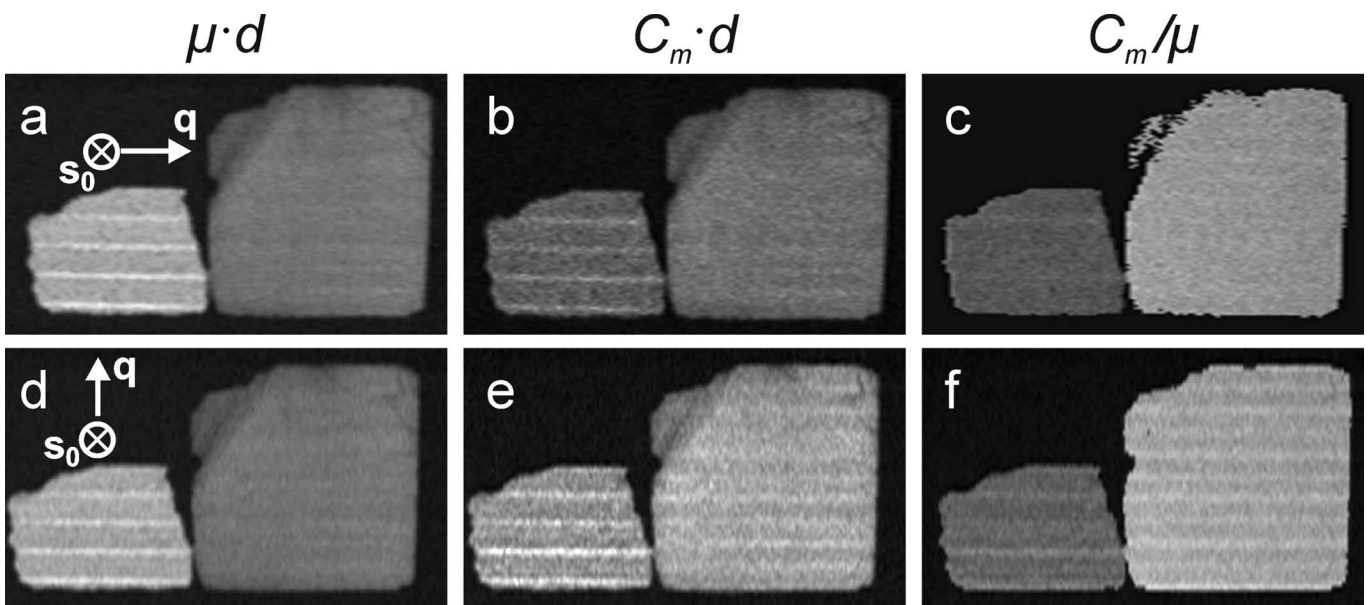


Fig. 5: Two-dimensional mapping of single wall slabs of cordierite samples. Large slab from sample S1, small slab from sample S2, respectively. The horizontal footprints indicate the extrusion direction. Top row: scattering vector q (nearly) parallel to extrusion, bottom row: scattering vector q perpendicular to extrusion. The incident beam direction s_0 is also indicated. The gray values correspond to: absorbing mass (a and d), volume-related specific surface (b and e), and mass-related specific surface (c and f).

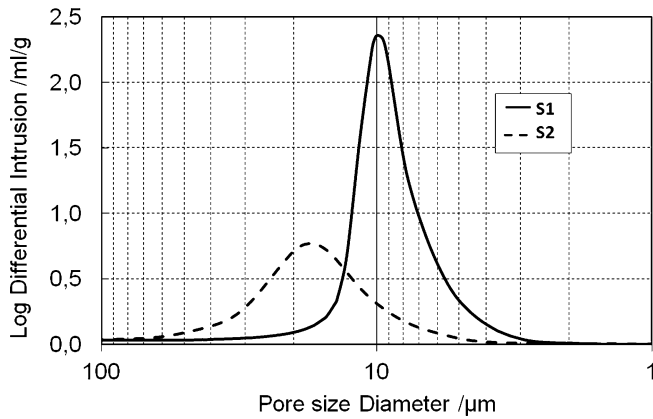


Fig. 6: Mercury intrusion pore size distribution plots for the two cordierite samples.

Table 3: Compilation of specific surface values of samples S1 and S2 for two perpendicular scattering directions relative to direction of extrusion.

C_m/μ	extrusion	⊥ extrusion
S1	2.02	2.2
S2	1.10	1.28
S1/S2	1.75	1.75

Quantitatively, the normalized refraction values C_m/μ (Figs. 5c and f), integrated over the whole sample area, are reported in Table 3. These values are relevant because they are independent of sample preparation (thickness), and yield two important pieces of information:

- They are higher in the direction perpendicular to extrusion. This implies that defect surfaces are preferentially aligned *along* the extrusion direction for both samples. The ratio of the refraction values parallel and perpendicular to the extrusion axis is also similar for both samples (Table 4), and quantitatively corresponds to the crystallographic texture values reported in 8.
- The ratios of the normalized refraction values between samples S1 and S2 are the same, in each scattering direction (Table 3). This implies that the pore microstructure (in particular, the pore morphology factor) of the two samples is similar, in spite of the size differences mentioned above.

Interestingly enough, the ratio of the refraction values (1.75) of the two samples corresponds to the ratio of the median pore diameters measured by means of mercury intrusion porosimetry (1.8). In spite of the approximations done in the mercury porosity analysis, the pore size having a limited meaning, this result implies that the refraction signal is indeed dominated by pore surfaces, and other defects contribute to a much lesser extent.

Fig. 7 shows synchrotron radiographs of the S1 slab at different angular positions of the analyzer crystal. The extrusion direction is always horizontal (and perpendicular to the scattering direction, also lying in the image plane). Fig. 7 also shows the Darwin-Prins rocking curves³⁷ of the analyzer crystal with (open squares) and without (solid line) specimen in the beam path (see Fig. 4). The image acquired at the top of the rocking curve is dominated by

absorption, but by tilting the analyser crystal off the specular reflection condition, it is possible to select only scattered (i.e. refracted) x-rays (this is analogous to moving the detector in the laboratory set-up).

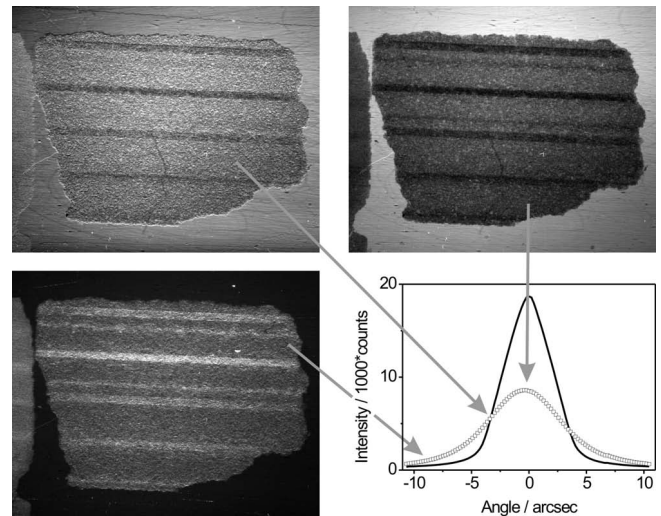


Fig. 7: Synchrotron radiographs of the S1 slab at different angular positions of the analyzer crystal. The extrusion direction is horizontal (i.e., perpendicular to the scattering direction, upwards within the sheet). Lower right: Darwin-Prins rocking curves³⁷ of the analyzer crystal with (open squares) and without (solid line) specimen in the beam path (see Fig. 4). The image contrast in the centre of the rocking curve is dominated by absorption (top right); the contrast is entirely reversed if the analyser crystal is tilted off center, thus accepting only scattered x-rays (bottom left).

Comparison of the laboratory refraction results with synchrotron refraction radiography provides additional evidence of the anisotropic pore morphology (interface orientation), with the advantage of higher spatial resolution. The ratio of the specific surfaces parallel and perpendicular to the extrusion axis exhibits similar values (it is even identical for sample S2, see Table 4). The slight differences can be explained with the different set-up: in the DEI (synchrotron) set-up a larger range of acceptance (scattering) angles is used.

Table 4: Specific surface ratios between the perpendicular and parallel directions (\perp/\parallel) with respect to the extrusion axis, for both S1 and S2.

C_m/μ	S1	S2
Laboratory	1.10	1.16
Synchrotron	1.06	1.15

The same kind of analysis can be applied to 2D tomographic images of the sample cross-sections (i.e., slices perpendicular to the extrusion axis, Fig. 8). Two types of images can be obtained separately: conventional density reconstructions (Fig. 8a, representing μ), and images of the specific surface (Fig. 8b, representing C_m). Reconstructions (Fig. 8) were performed with our in-house-developed DIRECTT^{45,46,47} algorithm.

Fig. 8a reveals an almost homogeneous density/porosity (at the given resolution of 50 μm) over the whole cross-section. Fig. 8b shows enhanced intensity at the surfaces.

This indicates artifacts arising from total reflection effects of plane surfaces (the walls). However, the reduced specific surface (i.e., C_m) in the wall-crossing areas does not seem to be an artifact, and can be explained with the presence of larger pores (assuming equal porosity in the two regions).

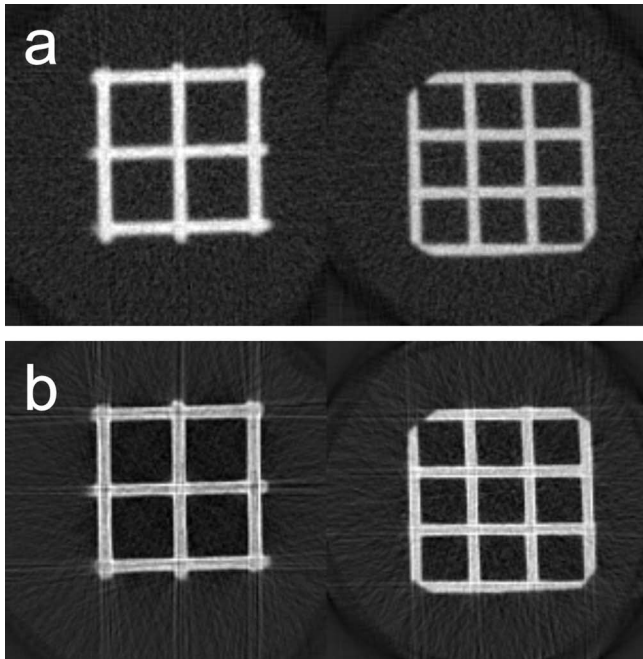


Fig. 8: 2D tomographic images of the sample cross-sections. Left: 4-channel sample S2, right: 9-channel sample S1. (a) Conventional density reconstruction (attenuation coefficient μ) and (b) reconstructions of the specific surface (refraction value C_m).

Again it should be noted that x-ray refraction is sensitive to interfaces. This implies that studying porosity or solid matter (particles) would yield the same results. This is not necessarily so for SEM or (absorption) CT data, pores and matter certainly not being the same object. Nevertheless, the good agreement of the present results with former Neutron Diffraction Texture Analysis⁸, with EBSD (electron back-scattering diffraction)⁷, and with mercury intrusion also implies that the salient microstructural features can be captured by means of analysis of *interfaces*. In Part 2 of this paper we shall show that three-dimensional methods (CT) and statistical analysis thereof yield very similar results, and therefore corroborate the experimental approach used in the present work.

V. Conclusions/Summary

In this work we have used x-ray refraction to characterize porosity and pore orientation in cordierite diesel particulate filter materials. The x-ray refraction has been implemented in different ways: simple scattering (OD), laboratory 2D mapping by sample scanning, 2D laboratory tomography, and full 2D imaging (refraction radiography) at a synchrotron source. We have found that all techniques yield the same result: the interface between pore and solid matter (to which x-ray refraction is sensitive) has a preferred orientation along the extrusion axis. This orientation factor (~ 1.2) agrees well with reported crystal texture values, and confirms that the interface density is the quantity of interest to characterize porosity in these materials. While x-ray absorption measurements yield a

value of the porosity in full agreement with classic mercury intrusion, the mean pore size determined by mercury porosimetry confirms the interface density ratio between the two cordierite samples found with x-ray refraction. Apart from environmentally friendly aspects, the refraction technique has a great advantage over classic mercury intrusion: it does not make any assumption with regard to the form of the pores. X-ray refraction is also virtually non-destructive, and can yield position-sensitive information, with a lateral resolution of about 100 μm , or even smaller if synchrotron radiation is used.

Acknowledgments

Amit Shyam (Oak Ridge National Laboratory), and Randy Stafford (Cummins Inc.) kindly provided the DPF samples.

References

- 1 Merkel, G., Tao, T.: Cordierite filters with reduced pressure drop. US patent 20040261384, (2006).
- 2 Readey, M.J., Rontanini, L.D.: Cordierite material useful in a heat source retainer and process for making the same. US Patent 4973566, (1990).
- 3 Saito, N., Nishimura, S.-Y., Kawano, M., Araki, S.-I., Suke-naga, S., Nakashima, K., Yasukouchi, T.: Fabrication of nitrogen-containing cordierite ceramics, *J. Am. Ceram. Soc.*, **93**, 2257–2263, (2010).
- 4 Bruno, G., Efremov, A.M., Clausen, B., Balagurov, A.M., Simkin, V.N., Wheaton, B.R., Webb, J.E., Brown, D.W.: On the stress-free lattice expansion of porous cordierite, *Acta Mater.*, **58**, 1994–2003, (2010).
- 5 Addiego, W.P., Melscoet-Chauvel, I.M.: High porosity cordierite ceramic article and method. US Patent 2007/0142208 A1, (2007).
- 6 Harada, T., Hamanaka, T., Hamaguchi, K., Asami, S.: Cordierite honeycomb-structural body and a method for producing the same. US Patent 4,869,944, (1989).
- 7 Bruno, G., Efremov, A.M., An, C.P., Wheaton, B.R., Hughes, D.J.: Connecting the macro and microscopic strain response in porous ceramics. part II microcracking, *J. Mater. Sci.*, **47**, 3674–3689, (2012).
- 8 Bruno, G., Vogel, S., Calculation of the average coefficient of thermal expansion in oriented cordierite polycrystals, *J. Am. Ceram. Soc.*, **91**, 2646–2652, (2008).
- 9 Hasselmann, D.P.H.: Unified theory of thermal shock fracture initiation and crack propagation in brittle ceramics, *J. Am. Ceram. Soc.*, **52**, 600–604, (1969).
- 10 Gulati, S.: Thermal stresses in ceramic wall-flow diesel filters. SAE technical paper 830079, (1983).
- 11 Bruno, G., Efremov, A.M., Webb, J.E.: The correlation between the coefficient of thermal expansion and the lattice mechanical properties of aluminum titanate, *Acta Mater.*, **58**, 6649–6655, (2010).
- 12 Bruno, G., Garlea, V.O., Muth, J., Efremov, A.M., Watkins, T.J., Shyam, A.: Temperature dependent microstress evolution in microcracked β -eucryptite, *Acta Mater.*, **60**, 4982–4996, (2012).
- 13 Shyam, A., Lara-Curzio, E., Pandey, A., Watkins, T.R., More, K.L.: The thermal expansion, elastic and fracture properties of porous cordierite at elevated temperatures, *J. Am. Ceram. Soc.*, **95**, 1682–1691, (2012).
- 14 ASTM standard C1198–01: Standard test method for dynamic young's modulus, shear modulus and poisson's ratio for advanced ceramics by sonic resonance, (2001).

- 15 Gibson, L.J., Ashby, M.F.: The mechanics of three-dimensional cellular materials, *P. Roy.Soc. Lond. A Mat.*, **382**, 43–59, (1982).
- 16 Bruno, G., Efremov, A.M., Levandovsky, A.N., Clausen, B.: Connecting the macro and microscopic strain response in porous ceramics: modeling and experimental validation, *J. Mater. Sci.*, **46**, 161–173, (2011).
- 17 Kachanov, M.: Effective elastic properties of cracked solids: a critical review of some basic concepts, *Appl. Mech. Rev.*, **45**, 304–335, (1992).
- 18 Kachanov, M.: Solids with cracks and non-spherical pores: proper parameters of defect density and effective elastic properties, *Int. J. Fract.*, **97**, 1–32, (1999).
- 19 Tandon, P., Heibel, A., Whitmore, J., Kekre, N., Chithrapragnada, K.: Measurement and prediction of filtration efficiency evolution of soot loaded diesel particulate filters, *Chem. Eng. Sci.*, **65**, 4751–4760, (2010).
- 20 Yang, J., Stewart, M., Maupin, G., Herling, D., Zelenyuk, A.: Single-wall diesel particulate filter (DPF) filtration efficiency studies using laboratory generated particles, *Chem. Eng. Sci.*, **64**, 1625–1634, (2009).
- 21 Andersson, L., Larsson, P.T., Wågberg, L., Bergström, L.: Evaluating pore space in macroporous ceramics with water-based porosimetry, *J. Am. Ceram. Soc.*, **96**, 1916–1922, (2013).
- 22 Lucas, R.: The time law of the capillary rise of liquids, (in German), *Kolloid Z.*, **23**, 15–22, (1918).
- 23 Washburn, E.W.: The dynamics of capillary flow, *Phys. Rev.*, **17**, 273–283, (1921).
- 24 Hentschel, M.P., Hosemann, R., Lange, A., Uther, B., Brückner, R.: Small angle x-ray refraction at metal wires, glass fibers and hard elastic polypropylene, (in German), *Acta Cryst. A*, **43**, 506–513, (1987).
- 25 Tzschichholz, G., Steinborn, G., Hentschel, M.P., Lange, A., Klobes, P.: Characterisation of porous titania yttrium oxide compounds by mercury intrusion porosimetry and x-ray refractometry, *J. Porous Mat.*, **18**, 83–88, (2011).
- 26 Silva, F.A., Williams, J.J., Müller, B.R., Hentschel, M.P., Portella, P.D., Chawla, N.: Three-dimensional microstructure visualization of porosity and Fe-rich inclusions in SiC particle-reinforced Al alloy matrix composites by x-ray synchrotron tomography, *Metall. Mater. Trans. A*, **41**, 2121–2128, (2010).
- 27 Shyam, A., Pandey, A., Bruno, G., Watkins, T.R., Lara-Curzion, E., Parten, R., Stafford, R.: In preparation (2013)
- 28 Pomeroy, M.J., O’Sullivan, D., Hampshire, S., Murtagh, M.J.: Degradation resistance of cordierite diesel particulate filters to diesel fuel ash deposits, *J. Am. Ceram. Soc.*, **95**, 746–753, (2012).
- 29 Bruno, G., Efremov, A.M., An, C.P., Nickerson, S.T.: Not all microcracks are born equal: thermal vs. mechanical microcracking in porous ceramics, In Widjaja, S., Singh, D. (Eds): Advances in bioceramics and porous ceramics IV - Ceramic engineering & science proceedings, **32**, 137–152, (2011).
- 30 Bruno, G., Pozdnyakova, I., Efremov, A.M., Levandovskiy, A.N., Clausen, B., Hughes, D.J.: Thermal and mechanical response of industrial porous ceramics, *Mater. Sci. Forum*, **652**, 191–196, (2010).
- 31 Bruno, G., Kilali, Y., Efremov, A.M.: Impact of the non-linear character of the compressive stress-strain curves on thermal and mechanical properties of porous microcracked ceramics, *J. Eur. Ceram. Soc.*, **33**, 211–219, (2013).
- 32 Bruno, G., Kachanov, M.: On modeling of microstresses and microcracking generated by cooling of polycrystalline porous ceramics, *J. Eur. Ceram. Soc.*, **33**, 1995–2005, (2013).
- 33 Glatter, O., Kratky, O.: Small angle x-ray scattering. Academic Press, London, 1982.
- 34 Harbich, K.-W., Klobes, P., Hentschel, M.P.: Microstructural characterization of porous materials by two-dimensional x-ray refraction topography, *Colloid. Surface A*, **241**, 225–229, (2004).
- 35 Müller, B.R., Lange, A., Harwardt, M., Hentschel, M.P., Illerhaus, B., Goebbels, J., Bamberg, J., Heutling, F.: Refraction computed tomography, *MP Mater. Test.*, **46**, 314–319, (2004).
- 36 Hentschel, M.P., Lange, A., Müller, B.R., Schors, J., Harbich, K.W.: x-ray refraction computer-tomography, (in German), *Materialprüfung*, **42**, 217–221, (2000).
- 37 Chapman, D., Thomlinson, W., Johnston, R.E., Washburn, D., Pisano, E., Gmür, N., Zhong, Z., Menk, R., Arfelli, F., Sayers, D.: Diffraction enhanced x-ray imaging, *Phys. Med. Biol.*, **42**, 2015–2025, (1997).
- 38 Pfeiffer, F., Weitkamp, T., Bunk, O., David, C.: Phase retrieval and differential phase-contrast imaging with low-brilliance x-ray sources, *Nature Phys.*, **2**, 258–261, (2006).
- 39 Ando, M., Maksimenko, A., Sugiyama, H., Pattanasiriwisawa, W., Hyodo, K., Uyama, C.: A simple X ray dark- and bright-field imaging using achromatic laue optics, *Jpn. J. Appl. Phys., Part 1*, **41**, L1016–L1018, (2002).
- 40 Strobl, M., Kardjilov, N., Hilger, A., Kühne, G., Frei, G., Manke, I.: High-resolution investigations of edge effects in neutron imaging, *Nucl. Instrum. Meth. A.*, **604**, 640–645, (2009).
- 41 Strobl, M., Hilger, A., Kardjilov, N., Ebrahimi, O., Keil, S., Manke, I.: Differential phase contrast and dark field neutron imaging, *Nucl. Instrum. Meth. A.*, **605**, 9–12, (2009).
- 42 Manke, I., Kardjilov, N., Schäfer, R., Hilger, A., Strobl, M., Dawson, M., Grünzweig, C., Behr, G., Hentschel, M., David, C., Kupsch, A., Lange, A., Banhart, J.: Three-dimensional imaging of magnetic domains, *Nature Commun.*, **1**, 125, (2010).
- 43 Lange, A., Hentschel, M.P., Kupsch, A., Müller, B.R.: Numerical correction of x-ray detector backlighting, *Int. J. Mat. Res.*, **103**, 174–178, (2012).
- 44 Kupsch, A., Hentschel, M.P., Lange, A., Müller, B.R.: How to correct x-ray detector backlighting, (in German), *MP Mater. Test.*, **55**, 577–581, (2013).
- 45 Lange, A., Hentschel, M.P., Kupsch, A.: Computed tomographic reconstruction with DIRECTT, (in German), *MP Mater. Test.*, **50**, 272–277, (2008).
- 46 Kupsch, A., Lange, A., Hentschel, M.P., Müller, B.R.: Improved computed tomography by variable desmearing, *MP Mater. Test.*, **52**, 394–400, (2010).
- 47 Lange, A., Kupsch, A., Hentschel, M.P., Manke, I., Kardjilov, N., Arlt, T., Grothausmann, R.: Reconstruction of limited computed tomography data of fuel cell components using direct iterative reconstruction of computed tomography trajectories, *J. Power Sources*, **196**, 5293–5298, (2011).

